Electrochimica Acta 507 (2024) 145109

Contents lists available at ScienceDirect

Electrochimica Acta

journal homepage: www.journals.elsevier.com/electrochimica-acta

One-pot synthesis of $FeNi_3/FeNiO_x$ nanoparticles for PGM-free anion exchange membrane water electrolysis

Francesko Malaj [a,b,*], Alessandro Tampucci [b], Domenico Lentini [b,c], Lorenzo Brogi [b], Enrico Berretti [d], Camilla Coletti [e,f], Stiven Forti [e], Antonio Rossi [e], Carlo Santoro [a,*]

[a] Electrocatalysis and Bioelectrocatalysis Lab, Department of Materials Science, University of Milano-Bicocca, Via Roberto Cozzi 55, Building U5, 20125, Milan, Italy
[b] Ne.m.e.sys. s.r.l., via 2 Giugno 8, 50019 Sesto Fiorentino, Fi, Italy
[c] Department of Chemical Sciences, University of Naples Federico II, Complesso Univ. M.S. Angelo, Via Cintia, IT-80126 Naples, Italy
[d] Istituto di Chimica Dei Composti OrganoMetallici (ICCOM), Consiglio Nazionale Delle Ricerche (CNR), Via Madonna Del Piano 10, Sesto Fiorentino, 50019, Firenze, Italy
[e] Center for Nanotechnology Innovation @NEST, Istituto Italiano di Tecnologia, P.zza S. Silvestro 12, 56127, Pisa, Italy
[f] Graphene Labs, Istituto Italiano di Tecnologia, Via Morego 30, 16163 Genova, Italy

ARTICLE INFO

Keywords:
AEM water electrolyzers
Platinum group metal-free
HER electrocatalysts
OER electrocatalysts

ABSTRACT

Low-temperature anion exchange membrane water electrolysis (AEMWE) is one of the most promising technologies to produce green hydrogen. To date, membrane-electrode assembly (MEA) based on platinum group metal (PGM) electrocatalysts shows higher performance than PGM-free ones. Here, a single and easy synthesis for non-noble metal electrocatalysts (PGM-free) for both hydrogen and oxygen evolution reactions (HER and OER) was developed. Both electrocatalysts consist of $FeNi_3/FeNiO_x$ nanoparticles obtained through chemical reduction using hydrazine. The electrocatalyst exhibits an overpotential of 210 mV and 234 mV for HER and OER respectively, at a current density of 10 mA cm^{-2} in 1 M KOH electrolyte, allowing a comparison between mass activity and geometric activity compared to PGM catalysts. In addition to a preliminary electrochemical characterization of the $FeNi_3/FeNiO_x$, the electrocatalyst were integrated into a pilot-scale AEMWE at both anode and cathode, which reaches (without iR-correction) 1.72 V and 1.94 V at a current density of 0.4 A cm^{-2} and 1 A cm^{-2} respectively at 60 °C. This PGM-free MEA outperforms the one based on Pt/C at cathode and RuO_2 at anode with a voltage gap of 284 mV at 1 A cm^{-2}. The aforementioned MEA was tested for 150 h with a discontinuous power profile, in order to get an idea of the possible degradation trends for a future industrial application, the reversible and irreversible voltage losses were calculated resulting in a degradation rate of 886 μV/h. This work demonstrates a simple and scalable synthesis of earth-abundant electrocatalytic materials for high-efficiency AEM water electrolysis.

1. Introduction

Electricity production plays a key role in modern society, its production from renewable sources and the parallel transition away from fossil fuels represents the turning point for environmental protection [1]. The use of renewable energies is expected to increase in the coming years, but these production methods suffer from intermittence issues due to daily, seasonal and regional factors. Often electricity from renewables is not absorbed by the grid and it is lost. To overcome those problems, hydrogen could be exploited as chemical storage due to its high energy density which makes it an excellent energy vector. Indeed, hydrogen can be obtained from surplus electricity and it can be stored, transported and reconverted into electricity on demand [2].

One of the most promising methods for hydrogen production is the water electrolysis operating at low temperatures. Nowadays, there are three different technologies that exploit this principle: proton exchange membrane water electrolysers (PEMWE), alkaline water electrolysers (AWE) and anion exchange membrane water electrolysers (AEMWE) [3].

PEMWEs have high efficiency, rapid response to load changes and are compatible with intermittent energy sources but requires expensive materials like platinum for electrocatalysts and fluorinated polymer membranes, in addiction to high corrosion problems due to acid environment [4].

* Corresponding authors.
E-mail addresses: f.malaj@campus.unimib.it (F. Malaj), carlo.santoro@unimib.it (C. Santoro).

https://doi.org/10.1016/j.electacta.2024.145109
Received 8 May 2024; Received in revised form 6 September 2024; Accepted 21 September 2024
Available online 22 September 2024

AWE is a mature technology for large-scale hydrogen production at low cost and high durability. Disadvantages are larger plant size, lower efficiency, not compatibility with intermittent energy sources and problems related to high corrosive environment due to the high concentrated electrolyte (up to 6–7 M KOH) [5].

AEMWEs combine the advantages of PEMWE and AWE technology named i) compatibility with intermittency renewable sources, ii) presence of solid polymeric membrane that guarantees physical separation with the possibility of pressurizing hydrogen internally, iii) low cost of electrocatalysts, iv) membranes that do not contain fluorinated polymers. Nowadays, the AEMWE technology is not used on a large scale due to problems mainly related to scarce durability of membranes and ionomers and to the low electrocatalytic activity of the electrocatalysts for both anodic and cathodic reactions, that lead to a lower efficiency compared to PEMWEs [6].

In the water electrolysis process, the reactions that take place respectively at the cathode side and at the anode side are the hydrogen evolution reaction (HER) and the oxygen evolution reaction (OER). Electrocatalysts are used to lower overpotentials and improve the electrocatalytic activity. Typical HER and OER reference electrocatalysts are platinum group metals (PGM), even in alkaline media. Particularly, RuO_2 and Pt supported over carbon (Pt/C) represent the most active electrocatalysts on AEM-WE for OER and HER, respectively [29,30]. Despite their excellent performance, they suffer from high costs and extreme scarcity as they are identified as critical raw materials (CRMs) by the European Union. These factors significantly limit their practicality and feasibility [3,7]. The substitution of these CRMs with more abundant and cheaper materials is a must for boosting up the massive deployment of this technology.

Among non-precious metal-based electrocatalysts, nickel-based materials have attracted attention for their low cost, conductivity and resistance to alkaline environments. Importantly, Ni belongs to the 10th group, sharing similar electronic structure with Pt and Pd. It's known that doping nickel-based electrocatalysts with heteroatoms or other metals can increase the electrocatalytic activity and an appreciated doping agent, due to its availability, is iron [8-10]

There are many works exploring electrocatalysts based on non-noble and earth-abundant metals such as nickel and iron for both HER and OER. Although many progresses have been made, they are currently unable to compete with PGM, both in terms of performance and durability [7,11,12].

Many synthetic strategies used in the literature to obtain nickel-iron electrocatalysts are based on electrodeposition [13]. Lian et al. obtained a Nickel-Iron (NiFe) electrocatalyst via high-current density electrodeposition that exhibited an overpotential of 100 mV at 10 mA cm^{-2} for HER in alkaline environment. Hatami et al. synthesized a Ni-Fe alloy on a Cu substrate via electrodeposition and tested it as a bifunctional HER/OER electrocatalyst for water spitting; this alloy showed overpotentials of - 124 mV at 10 mA cm^{-2} for the HER and 292 mV at 10 mA cm^{-2} for the OER. Luo et al. reported electrodeposition of NiFe nanosheets film on Ni foam (NiFe/NF) as a bifunctional electrocatalyst (HER/OER), resulting in overpotentials of - 139 mV at 10 mA cm^{-2} for the HER and 240 mV at 20 mA cm^{-2} for the OER [14-16]. Although electrodeposition is an effective technique, it's difficult to scale up due to limitations related to geometry and distance between electrodes. Recently the $FeNi_3$ alloy is attracting attention for its promising electrocatalytic activity for both HER and OER reactions [17-20]. The most common synthetic route for the $FeNi_3$ alloy is hydrothermal synthesis, for example Wei et al. first obtained $FeNi_3$-layered double hydroxide (LDH) nanosheets by reducing the nickel and iron salt in an autoclave at 120 °C for 12 h and then treated them with CH_4 plasma to support them on carbon and switch from face-centered cubic phase (fcc) to hexagonal close-packed (hcp). The latter showed higher activity with overpotentials of 70 mV for HER and 201 mV for OER at 10 mA cm^{-2} [21]. A simpler method to synthesize these materials could be obtained by the chemical reduction at low temperature of Nickel and Iron salts in aqueous solution using reducing agents. In particular, this procedure could lower costs and allow the mass production of electrocatalysts for green hydrogen. Sodium borohydride and hydrazine are common reducing agents used to obtain metal nanoparticles, although it is known that borohydride ions mainly give metal borate especially when water is used as a solvent [22]. Lu et al. first reported the synthesis of $FeNi_3$ nanoparticles in aqueous solution with hydrazine and recently other authors used this synthetic strategy to obtain electrocatalyst [23-25].

In literature, diverse Ni-based electrocatalysts that are integrated into completely PGM-free membrane electrode assembly (MEA) are reported and tested in AEMWE. Chen and Hu, prepared a NiMo electrocatalyst by reduction in a NH_3/H_2 atmosphere at high temperature and used it as is for HER and doped it with Fe via an anodic oxidation for OER. The single cell AEMWE with their PGM-free MEA reaches 1.57 V at 1 A cm^{-2}, with an operating temperature of 80 °C [26]. Wang et al. synthesized a Ni/Mo_5N_6 electrocatalyst, prepared by reduction in a NH_3/H_2 atmosphere at high temperature, as both anode and cathode; their cell also reached 1.57 V at 1 A cm^{-2} (operating temperature of 80 °C) [27]. Guo et al. prepared Fe_2P-$Ni_{12}P_5$ and Co_2P-$Ni_{12}P_5$ through electrodeposition method and used it as OER and HER respectively reaching 1.95 V at constant current density of 1 A cm^{-2} and with a temperature of 60 °C [28].

Here, we report a study related to the synthesis and characterization of $FeNi_3/FeNiO_x$ nanoparticles for both HER and OER. These materials were obtained via a feasible synthesis in aqueous solution with hydrazine. The developed synthesis allows to obtain nanoparticles with an average size of 70 nm. These nanoparticles were characterized microscopically and spectroscopically by means of High-resolution transmission electron microscopy (HRTEM), High-Angle Annular Dark Field scanning transmission electron microscopy (HAADF-STEM), X-ray photoelectron spectroscopy (XPS), X-ray diffraction (XRD), X-ray fluorescence (XRF), and scanning electron microscope (SEM). They were subsequently used to create electrodes capable of performing HER and OER reactions in an AEMWE and an accurate evaluation of the performance was obtained by comparing the voltage of the various set-ups at the same current density and temperature. We chose to carry out these tests in a pilot-scale electrolyzer (50 cm^2 of active area) to better evaluate, preliminarily, the possible future industrial application of electrocatalysts. The resulting $FeNi_3/FeNiO_x$ nanoparticles exhibits an overpotential of 210 mV and 234 mV for HER and OER respectively, at a current density of 10 mA cm^{-2}. The AEMWE tests using the PGM-free MEAs resulted in 1.72 V and 1.94 V at a current density of 0.4 A cm^{-2} and 1 A cm^{-2} respectively. These performances, although with a higher catalyst loading, were better than the ones obtained with MEAs based on PGM electrocatalysts especially MEAs containing Pt/C (cathode) and RuO_2 (anode) with a voltage gap of 284 mV at 1 A cm^{-2}. A concise study on the degradation trends was conducted by observing the response of the MEA to a power profile similar to that of renewable sources, a test with a daily power profile, resulting in a degradation rate of 886 μV/h over a total of 150 operational hours. This study paves the way for the use of the same nickel-based electrocatalysts for both HER and OER reactions, a favourable situation in terms of scalability and industrial flexibility, to obtain a high-performance, totally PGM-free MEA for green hydrogen production.

2. Materials and methods

2.1. Reagents

Iron (II) chloride tetrahydrate ($FeCl_2 \cdot 4\ H_2O$), nickel (II) chloride hexahydrate ($NiCl_2$ 0·6 H_2O), ruthenium (IV) (RuO_2, 99.9 % metals basis), platinum supported on carbon Pt/C (40 wt %), hydrazine hydrate (N_2H_4 50–60 % water solution), $NaBH_4$, ethanol, PolyVinil Alcohol (Mw 89,000–98,000, 99 % hydrolyzed), Polytetrafluoroethylene 60 wt % dispersion in H_2O, sodium hydroxide (NaOH, 98 %), potassium hydroxide (KOH, purity 85 %) and polyvinylpyrrolidone (PVP, M.W.

40.000) were purchased from Sigma-Aldrich and used as received without further purification. carbon cloth porous transport layer (0.410 mm thickness, Xiamen Zopin New Material Limited, China); Nickel foam (1.5 mm, Xiamen Tmax Battery Equipments Limited, China).

Binder (Ethanolic solution 10% w/v) and the anion exchange membranes utilized in the study (AT-100), was kindly supplied by Ne.m.e.sys. s.r.l. (Italy).

2.2. Synthesis $FeNi_3/FeNiO_x$ NPs

$FeNi_3/FeNiO_x$ nanoparticles (NPs) were synthesized through a chemical reduction method. 10 g of $NiCl_2$ 0·6 H_2O (42 mmol), 2 g of $FeCl_2 \cdot 4\ H_2O$ (10 mmol), and 7 g of PVP were dissolved in 300 ml of water. The mixture was stirred for 10 min and then heated to reach 70 °C. A second solution of 100 mg of $NaBH_4$ (2.6 mmol), 6 g of NaOH (150 mmol), and 30 ml of hydrazine solution was prepared and mixed with the first one.

After mixing the two solutions, a black solid dispersed in the reaction mixture and gas was formed, indicating the formation of $FeNi_3/FeNiO_x$ nanoparticles. The reaction was kept a 70 °C until the solution turns colourless. The nanoparticles were recovered and washed five times with water aliquots of approximately 100 mL to remove byproducts and PVP, then were washed and stored in ethanol.

2.3. Preparation of electrode

2.3.1. Preparation of the standard electrodes

The anode electrode for the LSV and test was manufactured as follow: 32 mg of RuO_2 powder were dispersed in 72 μL of the binder ethanolic solution. The ink was spread onto 8 cm^2 of Nickel foam and dried in an oven overnight at 30 °C. The final electrocatalyst loading was 4 mg cm^{-2}.

The anode electrode for the cell test was manufactured as follow: 200 mg of RuO_2 powder were dispersed in 448 μL of the binder ethanolic solution. The ink was spread onto 50 cm^2 of Nickel foam and dried in an oven overnight at 30 °C. The final electrocatalyst loading was 4 mg cm^{-2}.

The cathode electrode for the LSV test was manufactured as follow: 10 mg of Pt/C powder was mixed, in an ultrasonic bath for 30 min, to 22,5 μL of the binder ethanolic solution. The ink was spread onto 8 cm^2 of Nickel foam and dried in an oven overnight at 30 °C. The final Pt loading was 0.5 mg cm^{-2}.

The cathode electrode for the cell test was manufactured as follow: 62,5 mg of Pt/C powder was mixed, in an ultrasonic bath for 30 min, to 140 μL of a 10% w/v aqueous solution of PolyVinil Alcohol. The ink was spread onto 50 cm^2 of carbon cloth porous transport layer (PTL) and dried in an oven overnight at 50 °C. The final Pt loading was 0.5 mg cm^{-2}.

RuO_2 as OER electrocatalyst and Pt/C as HER electrocatalyst were selected as benchmark for their reactions in alkaline media [29,30].

2.3.2. Preparation of the $FeNi_3/FeNiO_x$ electrode

The anode electrode the LSV test was manufactured as follow: 200 mg of $FeNi_3/FeNiO_x$ powder were dispersed in 800 μL of ethanol and 36 mg of the aqueous dispersion of Polytetrafluoroethylene (60 wt%) were added. The ink was manually spread onto 8 cm^2 of Nickel foam and dried in an oven overnight at 30 °C. The final electrocatalyst loading was 25 mg cm^{-2}.

The anode electrode for the cell test was manufactured as follow: 1.25 g of $FeNi_3/FeNiO_x$ powder were dispersed in 5 mL of ethanol and 0.230 g of the aqueous dispersion of Polytetrafluoroethylene (60 wt%) were added. The ink was manually spread onto 50 cm^2 of Nickel foam and dried in an oven overnight at 30 °C. The final electrocatalyst loading was 25 mg cm^{-2}.

The cathode electrode for the LSV test was manufactured as follow: 200 mg $FeNi_3/FeNiO_x$ powder were mixed, in an ultrasonic bath for 30 min, to 448 μL of the binder ethanolic solution. The ink was manually spread onto the 8 cm^2 of Nickel foam and dried in an oven overnight at 30 °C. The final electrocatalyst loading was 25 mg cm^{-2}.

The cathode electrode for the cell test was manufactured as follow: 1.25 g $FeNi_3/FeNiO_x$ powder were mixed, in an ultrasonic bath for 30 min, to 2.8 mL of a 10% w/v aqueous solution of PolyVinil Alcohol. The ink was manually spread onto the 50 cm^2 of Carbon Cloth Gas Diffusion Layer and dried in an oven overnight at 30 °C. The final electrocatalyst loading was 25 mg cm^{-2}.

2.4. Electrochemical measurements

A conductivity (σ) measurement was obtained by pressing 4.7 g of powder inside a hydraulic press with 13 mm diameter steel pistons (Silfradent, Italy) with a pressure of 368 MPa to have a good compaction degree of the particles and ensure electrical contact. The resulting tablet was homogeneous and cylindrical in shape with a diameter equal to that of the pistons and a height (h) of 8.6 mm. It was placed between two nickel foils, to distribute the current homogeneously and axially inside the cylinder, and the electrical 4-point measurements were performed at room temperature with an Hioki 3560 AC mW HiTester, with AC perturbation at 1 kHz (Hioki Corporation, Japan).

σ was calculated from the corresponding resistance (R) by using the following equation Eq. (1):

$$\sigma = \frac{h}{RA} \tag{1}$$

Where (A) is the base area of the cylinder.

The OER and HER tests were carried using a three-electrode system, using a reversible hydrogen electrode (RHE) Mini HydroFlex 80,521 (Gaskatel, Germany) as the reference.

Linear sweep voltammetry (LSV) curves were obtained with an Arbin BT-G battery testing workstation (USA) by applying a scan rate of 5 mV s^{-1} under continuous stirring at 600 rpm to prevent gas bubble accumulation on the electrodes at room temperature. Prior to recording the LSV curves, electrode activation was performed through cyclic voltammetry (CV) in a potential window ranging from 1.2 V to 1.8 V vs RHE for OER and from 0.02 V to −0.6 V vs RHE for HER at 50 mV s^{-1} until a stable CV was achieved. Electrocatalyst overpotentials were determined from the recorded LSV curves at a current density of 10 mA cm^{-2}.

Overall water electrolysis tests were performed in a single cell AEMWE with an active area of 50 cm^2 (SCBT-100, Nemesys s.r.l.) comprising of stainless-stell end plates, bipolar plate and a plastic frame. The performance of the $FeNi_3/FeNiO_x$ electrocatalyst developed in this study have been compared to platinum on carbon (Pt/C) as HER and RuO_2 as OER, through the acquisition of polarization curves at 50 °C and 60 °C.

The MEA was formed by mechanically compression of the AT-100 membrane sandwiched between anode and cathode at a pressure of 2 MPa. The membrane was previously activated in a 1 M KOH aqueous solution for 24 h reaching a thickness of 60 μm. Electrodes were previously activated in a 1 M KOH aqueous solution for 30 min.

Electrolyte was 1 M KOH aqueous solution supplied by a peristaltic pump with a flow rate of 200 mL/min.

Polarization curves were obtained by applying current steps while iR-Free voltages were measured on-line by AC perturbation at 1 kHz (Hioki 3560 AC mW HiTester, Hioki Corporation, Japan); varying the temperature of a 1 M KOH aqueous solution supplied by the peristaltic pump.

Finally, an analysis of the degradation trend of $FeNi_3/FeNiO_x$ MEA with an intermittent power supply was conducted. The test was performed at a current density of 0.4 A cm^{-2}, at 50 °C. Daily power supply varied between a minimum of 8 h and a maximum of 17.5 h, maintaining at least 8 h of OCV between one day and the next. All electrochemical measurements were conducted in an alkaline electrolyte (KOH 1 M).

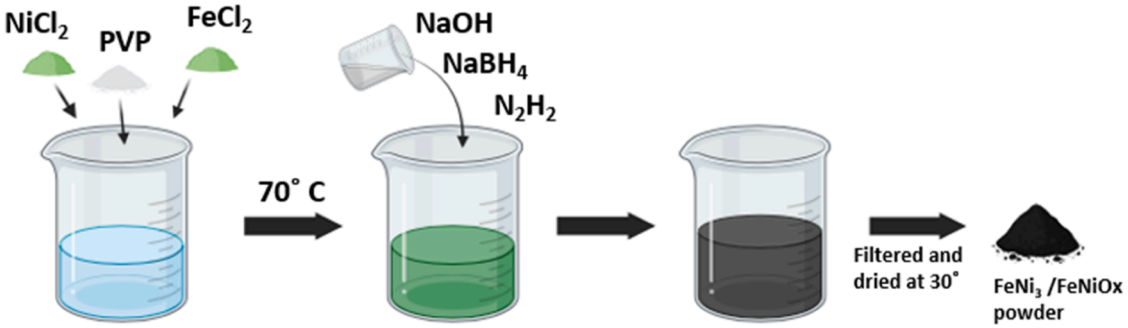

Fig. 1. Synthesis of $FeNi_3/FeNiO_x$.

2.5. Characterization methods

2.5.1. XPS analysis

The measurements were performed using a Specs XR50 source with an Al anode at a power of 300 W. The analyser employed was a Specs Astraios 190 with a 2D-CMOS detector and a 1.5 × 25 mm entrance slit. High-resolution spectra were acquired with a pass energy of 10 eV, while a pass energy of 50 eV was utilized for the survey. The photoemission angle at which the measurements were taken was 25°

The Ni 2p and Fe 2p spectra were fitted first by calculating the Shirley background and then using a linear combination of Gaussian-Lorentzian sum (GLS) doublets and single GLS. The GLS functions are symmetric and characterized by a single parameter to describe the full width at half maximum (FWHM). The components are explicitly shown in the plot, together with the resulting envelope function.

2.5.2. XRD analysis

X-ray diffraction (XRD, Rigaku Miniflex 600) equipped with a copper source was used to perform crystallographic investigations in the 2θ range of 10–90°

2.5.3. XRF analysis

Inorganic elemental analysis was qualitatively carried out using X-rays fluorescence (XRF, Artax 200, Bruker, Billerica, MA, USA) having Mo anode.

2.5.4. SEM analysis

For the morphological analysis of the electrocatalyst, a desktop scanning electron microscope (SEM, Thermo Fisher Phenom G6, Eindhoven, The Netherlands) equipped with a thermionic CeB6 source was employed. The instrument operates in the magnification range of 400 – 70,000 x.

2.5.5. HRTEM analysis

HRTEM images were acquired using a Thermofisher Talos F200X G2 at an accelerating voltage of 200 kV using a high-speed CETA camera operating at a camera resolution of 4096 × 4096 pixels without any objective aperture. The High-Angle Annular Dark Field images were acquired with a Panther annular STEM detector using a convergent beam with an angle of 10.5 mrad and a camera length of 330 mm. The EDX maps were taken with a Super X spectrometer equipped with four 30 mm^2 silicon drift detectors with a collection angle of 0.7 srad.

3. Results and discussion

3.1. Synthesis and characterization

The synthetic process is here described step by step. Hydrazine in alkaline solutions can acts both as a reductant or an oxidant according to the following reactions reported in Eqs. (2) and Eq. (3):

$$N_2H_4 + 4\ OH^- \rightarrow N_2 + 4\ H_2O + 4\ e^- \quad (2)$$

$$N_2H_4 + 2\ H_2O + 2\ e^- \rightarrow 2\ NH_3 + 2\ OH^- \quad (3)$$

It is known that Ni^{2+} can be easily reduced in alkaline aqueous solutions of hydrazine while this is not possible for Fe^{2+} alone due to its greater tendency to oxidize to Fe^{3+}. Despite this, as reported by Lu et al. [25], when Ni^{2+} and Fe^{2+} coexist in solution, the preliminary reduction of nickel by hydrazine forms nuclei which catalyse the reduction of Fe^{3+}, allowing to obtain Ni_3Fe alloy as reported in Eq. (4):

$$3\ Ni^{2+} + Fe^{2+} + 2\ N_2H_4 + 8\ OH^- \rightarrow Ni_3Fe + 2\ N_2 + 8\ H_2O \quad (4)$$

In this study, we used polyvinilpirrolidone as a surface stabilizer to minimize particle aggregation and control the nucleation rate [31]. A small amount of $NaBH_4$ was dissolved in the hydrazine solution as inducing agent which, as suggested by Li et al. [32], form Ni-B species that speed up the formation of the first Ni^0. They catalyse the formation of further Ni^0 which, in turn, catalyses the formation of the Ni_3Fe alloy [32] (Fig. 1).

The nanoparticles formation, in addition to being an autocatalytic reaction, catalyses two other reactions involving hydrazine: its decomposition reported in Eq. (5) and its disproportionation shown in Eq. (6).

$$N_2H_4 \rightarrow N_2 + H_2 \quad (5)$$

$$3\ N_2H_4 \rightarrow N_2 + 4\ NH_3 \quad (6)$$

For this reason, during the reactions, gas is produced simultaneously with the formation of a fine black powder.

Although from a molecular point of view numerous reactions occur simultaneously, macroscopically everything occurs with a single addition in a single reactor. The reaction is complete within a few minutes with a yield of 99 % and is followed by a rapid work-up (filtering and drying), as shown in Fig. 1.

As previously reported by Lu et al. [25] an Ni/Fe molar ratio <3 leads to the simultaneous presence of $FeNi_3$ alloy and crystalline Fe_4O_3 in the nanoparticle while a molar ratio equal to 3 would lead only to the $FeNi_3$ alloy. To obtain an amorphous component inside the nanoparticle we tried a Ni/Fe molar ratio of 4, an excess of nickel compared to that needed to obtain the alloy, and this allowed the simultaneous co-presence of amorphous nickel and iron oxides both inside and over the surface of the nanoparticles. This particular situation can increase the electrocatalytic activity towards HER and OER [33,34,46-48].

The XRF analysis was done to evaluate the presence of the metal of interest and confirmed the presence of both nickel and iron. (Figure S1, supporting information).

SEM images shows how, on a micrometer scale, $FeNi_3/FeNiO_x$ powder forms agglomerates, favoured by their magnetic properties (Figure S2 (a), supporting information). This agglomerate has a "spongy" shape. The images of the powder smeared on the electrodes. (Figure S2 (b), supporting information) shows the complete coverage of the GDL. This can be attributed to the high compatibility between the binder and the electrocatalyst, which allows the formation of a uniform mixture and

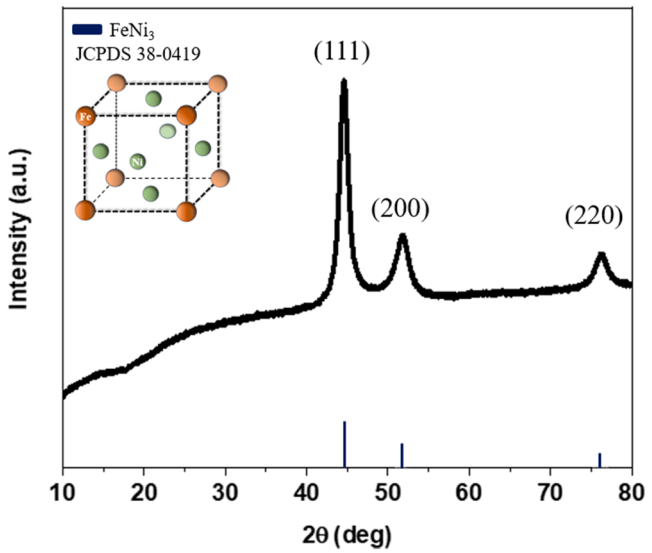

Fig. 2. XRD spectrum of the nanoparticles obtained.

allows effective adhesion to the surface. The same electrodes seen at higher magnification in present fractures, roughness, and inhomogeneity (Figure S2 (c), supporting information). These situations are advantageous since they increase the surface area which activates the mass transfer and also the transfer of the gaseous products released by the electrocatalyst and favours the evolution reaction of oxygen and hydrogen [35].

The XRD pattern (Fig. 2) displays three peaks at Bragg angles of approximately 44°, 51.3°, and 75.6°, respectively, in good agreement with the standard patterns of $FeNi_3$ (JCPDS Card No 38–0419, Awarite). For each reflection, the corresponding crystallographic plane family has been indicated using Miller indices and interplanar distance. The Miller indices (111), (200), and (220), with interplanar distances of 2.05 Å, 1.77 Å, and 1.25 Å, respectively, confirm the presence of $FeNi_3$ with a face-centered cubic (FCC) structure, where Ni atoms occupy the face centers and Fe atoms reside at the corners [32]. The broadened reflections indicate that the average crystal diameter is on the order of nanometers.

Furthermore, from the analysis of the diffractogram, it is possible to observe a highly modulated background and the presence of broadened reflections. Hence, the presence of amorphous phases could be hypothesized, which cannot be identified based exclusively on XRD analysis [36].

High resolution transmission electron microscope (HRTEM) (Fig. 3) shows that the average particle size is 70 nm, spherical and uniformly distributed, displacing the lattice spacing of 0.205 nm, and 0.177 nm corresponding to the (111) and (200) planes of Ni_3Fe with FCC structure, in agreement with the result of XRD.

STEM-EDX (Fig. 4) mapping images also indicate the uniform dispersion of Ni, Fe and O elements on the nanoparticles and reports that the Ni/Fe molar ratio inside the particles is approximately 4, in line with the one used during the synthesis. Linescan analysis (Fig. 5) also shows a constant concentration of oxygen within the particles with an increase closer to the surface. By combining this information with that given by the XRD it is possible to hypothesize that inside the particles, together with the Ni_3Fe alloy, uniformly distributed amorphous zones of Ni and Fe with higher oxidation states coexist. From the EDX mapping reported in Figure S3 (supporting information) the presence of boron can be excluded, even the nitrogen signal is too small to confirm its actual presence, and certainly makes impossible its quantification with respect to the other elements. Considering that carbon counting cannot be performed from Figure S3 (supporting information) because a carbon substrate was used to fix the nanoparticles during the HR-TEM analysis, the presence of PVP can be excluded by comparing the FT-IR spectra reported in Figure S4 (supporting information). Combining this information, we can exclude that traces of by-products and PVP remain in the electrocatalyst powder, presumably removed during the water washings after the synthesis.

In Fig. 6, we display the core level spectra recorded on samples of pure Fe and Ni powders, respectively. For fitting the data gathered on the Fe 2p, we used a Shirley background, which came at convergence after four iterations. The shape of the peak reveals a dent at 707.3 eV, which we assign to metallic – Fe^0 – iron. Considering how embedded the metallic contribution is in the convolution of the other components, we used a symmetric doublet to represent it. In addition, it is known that the metallic peak is accompanied by an energy-loss peak at about 6 eV, which we include in the fit as well. The rest of the Fe 2p is represented by higher oxidation states components, namely Fe^{2+} at and Fe^{3+} [37]. Finally, to account for the shape of the spectrum at energies below 707 eV, a so-called pre-peak contribution needed to be introduced, as indicated in previous works [38].

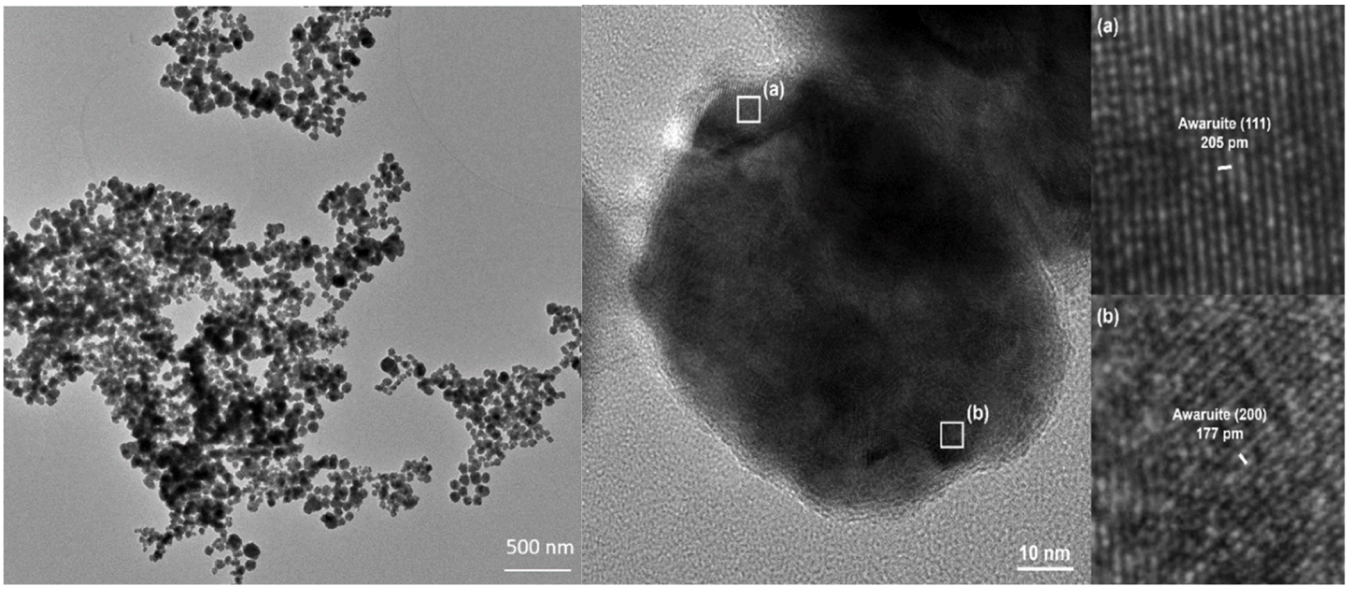

Fig. 3. (a) HR-TEM image of $FeNi_3/FeNiO_x$ at a magnitude of 500 nm **(b)** Lattice fringe pattern of $FeNi_3/FeNiO_x$.

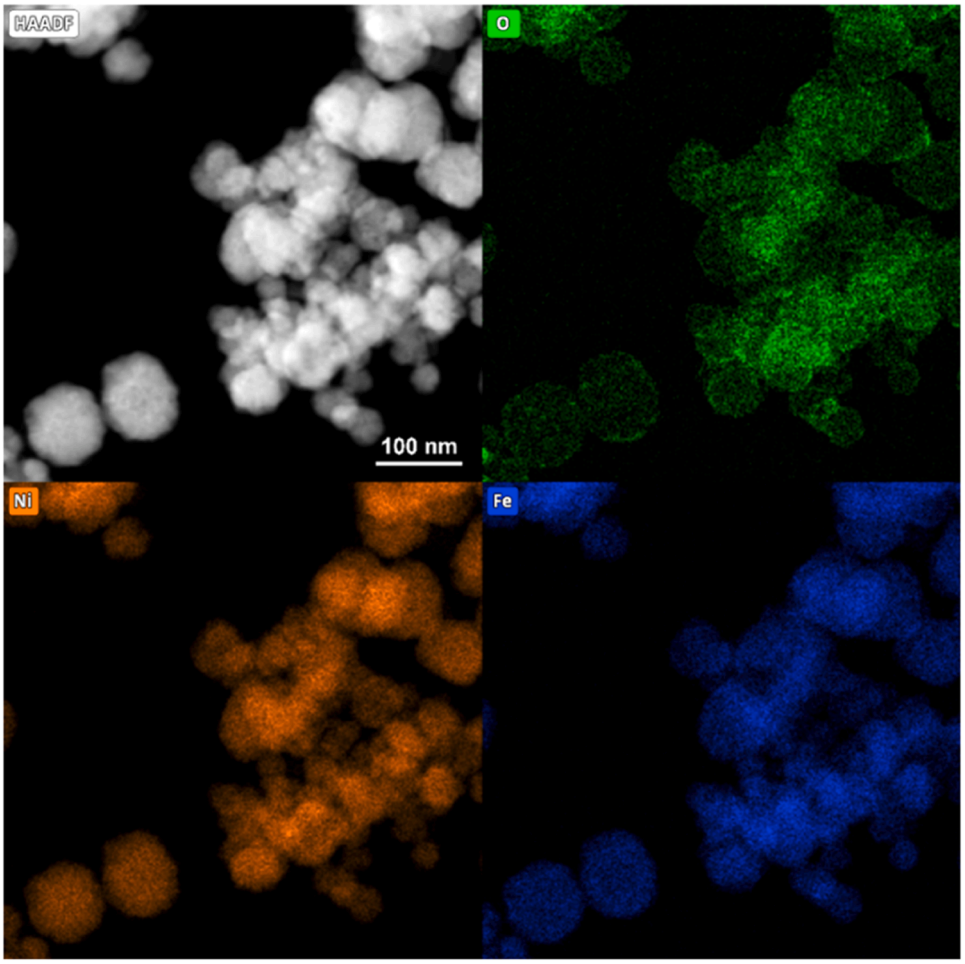

Fig. 4. EDX mapping images of $FeNi_3/FeNiO_x$.

The Ni 2p peak in Fig. 6(b) was as well fitted starting from a Shirley-type background contribution, as widely utilized in the literature. The Ni 2p peak is known to be difficult to fit and to be interpreted. Following previous works reported in the literature [39], we assign the metallic (Ni^0) component at 852.7 eV. A plasmon peak at +6 eV is associated with it. The successive contribution is ascribed to nickel hydroxides NiOOH and it is associated with two components at 854.4 and 856.2 eV, respectively [40]. The higher energy components are assigned to Ni $(OH)_2$ at 861.4 eV and one to NiO at 863.4 eV. The relative concentration of metallic element in each compound was then found as 23 % for Fe and 20 % for Ni.

Given the simultaneous presence of the $FeNi_3$ alloy and higher oxidation states for the metals both in the core and on the surface, it was chosen to rename the nanoparticles obtained as $FeNi_3/FeNiO_x$.

From the HAADF-STEM analysis of three different nanoparticles we can approximate an average molar ratio of nickel, iron and oxygen within the nanoparticles equal to 4:1:0.6 respectively. Using these stoichiometric ratios in the product it is possible to calculate the yield of the reaction by comparing, for three different batches, the weight of the metal salts added compared to the weight of the final washed and dried powder. From the results shown in Table S1, supporting information, it is possible to approximate a reaction yield of 99 %

3.2. Electrochemical activity

A measure of the electrical conductivity of $FeNi_3/FeNiO_x$ powder was made as reported in "materials and methode", obtaining a value of $3.2{\cdot}10^2\ \Omega^{-1}m^{-1}$. This result agrees with the ranges present in the literature for other NiFe alloys and for benchmark RuO_2 [56,57]. The activities of the $FeNi_3/FeNiO_x$ electrocatalysts for both HER and OER reactions were firstly investigated using linear sweep voltammetry in 1 M KOH electrolyte in a standard three-electrode system and information on the kinetics was obtained thanks to the Tafel slopes analysis. Commercial RuO_2 and Pt/C were chosen as the benchmark electrocatalyst for OER and HER respectively and electrochemically evaluated under the same conditions for comparison. Electrocatalysts loading onto the electrodes surface were the same for every set-up, as reported previously in materials and methods Section. To comprehensively evaluate the applicability of $FeNi_3/FeNiO_x$ for low-temperature water electrolysis tests were carried out in a single-cell AEMWE in which the performances were evaluated through the acquisition of polarization curves at 50 °C and 60 °C with KOH 1 M as supporting electrolyte. Given the greater availability of reagents, the low cost and the ease of synthesis of $FeNi_3/FeNiO_x$ nanoparticles, a higher catalyst loading was used compared to that of the benchmark PGMs, considering it a more plausible situation from an industrial point of view. In any case an evaluation of the catalytic activity per unit mass (mass activity) versus geometric activity [58] is reported in Fig. 9, Figure S5 and S6, supporting information.

3.3. Oxygen evolution reaction of $FeNi_3/FeNiO_x$ electrocatalysts

The polarization curves of $FeNi_3/FeNiO_x$ and RuO_2 for the OER were provided in Fig. 7. $FeNi_3/FeNiO_x$ nanoparticles demonstrated higher OER activity with an overpotential of 234 mV at the benchmark current density of 10 mA cm^{-2}. The overpotential of the RuO_2 measured in the

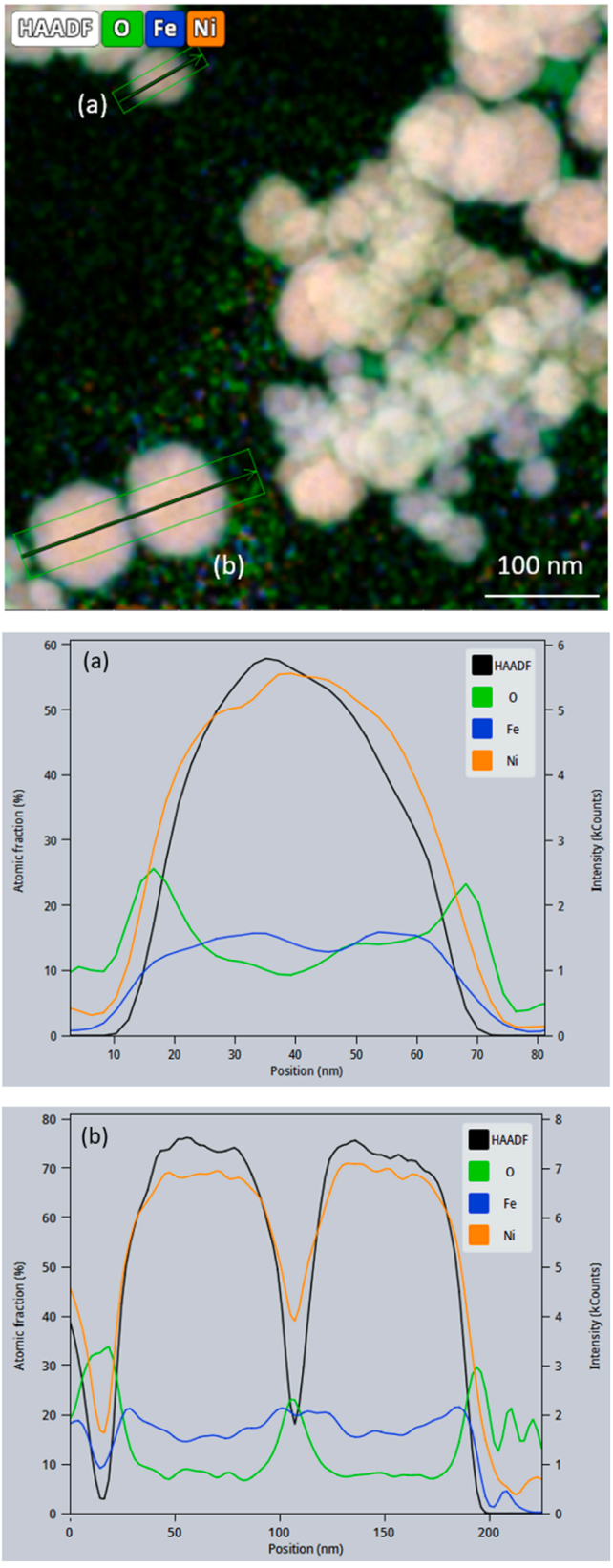

Fig. 5. HAADF-STEM of $FeNi_3/FeNiO_x$ and relative atomic fraction of the elements in the $FeNi_3/FeNiO_x$ nanoparticle.

same conditions was found to be 307 mV, therefore a gap of 73 mV was highlighted Fig. 7(a). We have also calculated the Tafel slopes of the two electrocatalysts to compare their kinetics features. Interestingly, the $FeNi_3/FeNiO_x$ plot has a lower slope than that of RuO_2, 80 $mVdec^{-1}$ versus 99 $mVdec^{-1}$, respectively, as shown in Fig. 7(b), highlighting a better kinetics towards the OER. Both electrocatalysts were also integrated into the cathode electrode and a MEA was fabricated and tested in a single AEMWE cell. The polarization curves in the AEMWE were run integrating the Pt/C at the cathode and comparing the $FeNi_3/FeNiO_x$ with the RuO_2 at the anode at 50 °C (Fig. 7c) and 60 °C (Fig. 7d) as operating temperature. For both temperatures, the voltage cell of $FeNi_3/FeNiO_x$, used as the electrocatalyst at the anode, is lower in the entire range of applied current density compared to the one produced by RuO_2 as anode electrocatalyst. The average voltage gap between the two curves at 50 °C is 260 mV, with an increasing trend with the current density. In fact, at 0.4 A cm^{-2}, the gap is 251 mV, which increases to 414 mV at 1 A cm^{-2}; demonstrating improved reaction kinetics for $FeNi_3/FeNiO_x$ at high current densities. Moreover, at 60 °C the kinetics shows the same pattern, with an average voltage gap of 228 mV and, in particular, at 0.4 A cm^{-2} the gap is 227 mV, which increases to 389 mV at 1 A cm^{-2}. The high OER electrocatalytic activities of $FeNi_3/FeNiO_x$ are consistent with previous studies on Ni-Fe oxide alloys [41,42,45]. The higher loading compared to RuO_2 must be considered, which compensates for its higher mass activity, allowing to obtain a higher geometric activity (Fig. 9 and Figure S5, supporting information). This is a common situation in the literature for PGM-free catalysts used for OER reactions in alkaline environments [58] and, at least in our case, a good compromise given the economic and practical aspects already mentioned for the synthesis of $FeNi_3/FeNiO_x$.

3.4. *Hydrogen evolution reaction of $FeNi_3/FeNiO_x$ electrocatalysts*

The polarization curves of $FeNi_3/FeNiO_x$ and Pt/C were provided in Fig. 8. In contrast on the results recorded for the OER, even with higher loading $FeNi_3/FeNiO_x$ does not outperform the PGM benchmark, for both mass activity and geometric activity (Fig. 9 and Figure S6, supporting information). As expected, the overpotentials at 10 mA^{-2} are 210 mV for $FeNi_3/FeNiO_x$ and 26 mV for Pt/C respectively and a gap of 184 mV was highlighted Fig. 10(a). Even the Tafel slop, shown in Fig. 8 (b), shows how Pt/C has a higher reaction kinetics than $FeNi_3/FeNiO_x$, 73 $mVdec^{-1}$ versus 176 $mVdec^{-1}$ respectively. This difference in the Tafel slope highlight a variation in the rate-determining step of the reaction, with lower hydrogen evolution rate on the electrode surface, suggesting a lower propensity for water breakdown and H adsorption on it (Volmer-Heyrovsky mechanisms). $FeNi_3/FeNiO_x$ and Pt/C were then integrated into the cathode of and AEMWE single cell and RuO_2 was used as anode electrocatalyst. Polarization curves were run for the single cell AEMWE at two different operating temperatures of 50 °C (Fig. 8c) and 60 °C (Fig. 8d). Also, the polarization curves of the AEMWE, fixing the RuO_2 as anode, highlighted the trend observed for the polarization curves of the single electrode. Here the average voltage gap between the two curves at 50 °C was 123 mV, the gap at 0.4 A cm^{-2} is 129 mV, which increases to 178 mV at 1 A cm^{-2} (Fig. 8c). At 60 °C, the average difference in cell voltage was measured as 152 mV (Fig. 8d), meanwhile is 150 mV at 0.4 A cm^{-2} and 173 mV at 1 A cm^{-2}. In this case, the curves show different trends compared to the OER, in fact the gaps between the curves of the two electrocatalysts present lower and more constant values, being less affected by the increase in temperature and current density. Unfortunately, for HER, at date, Pt/C seems to be the best option to pursue and a gap with other PGM-free electrocatalyst still remains. This is not surprising, given that the electrocatalytic activity for the reaction of HER is strongly influenced by the hydrogen adsorption capacity. Therefore, a suitable electrocatalyst should bind to the reaction intermediates neither too strongly nor too weakly, following the Sabatier principle, so as to balance the adsorption (activation process) and desorption (hydrogen release), ensuring maximum activity,

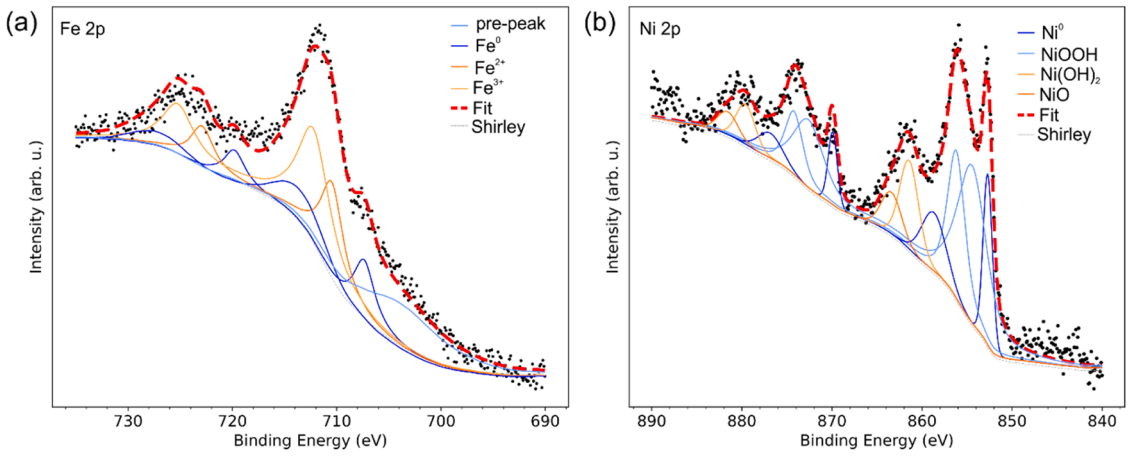

Fig. 6. XPS spectra of $FeNi_3/FeNiO_x$ (a) Fe 2p and (b) Ni 2p core levels.

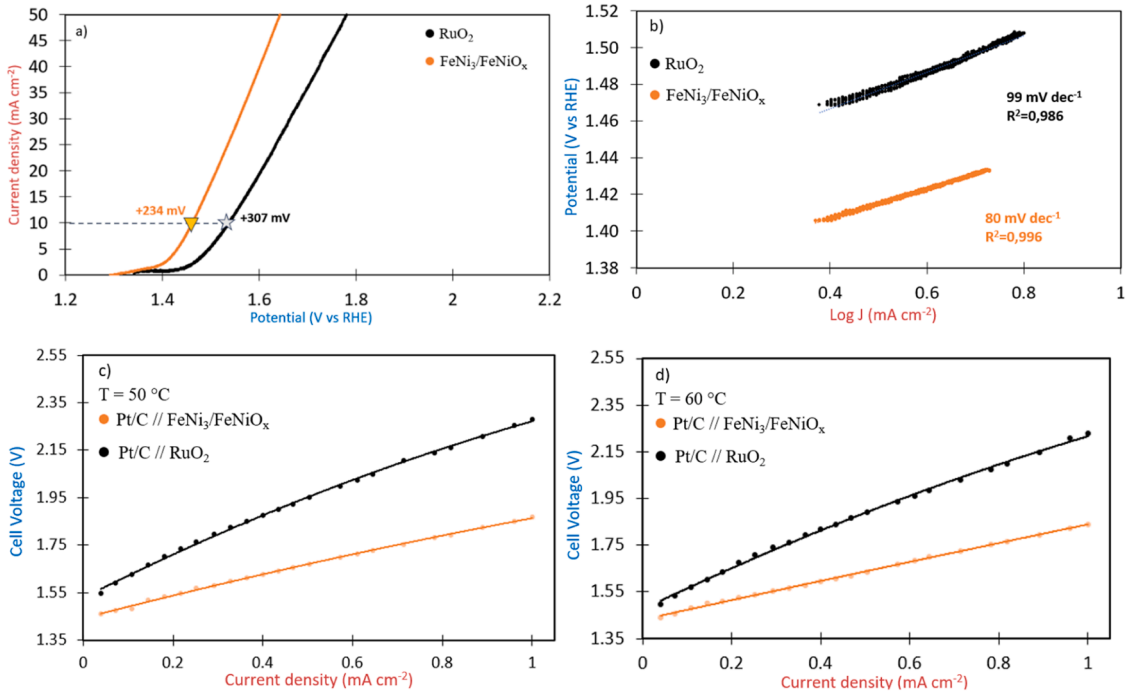

Fig. 7. (a) LSV comparison of OER electrocatalysts in 1.0 M KOH solution at a sweep rate of 5 mV s^{-1}: $FeNi_3/FeNiO_x$ (orange curve), RuO_2 (black curve). (b) Tafel Plot comparison of OER electrocatalysts: $FeNi_3/FeNiO_x$ (orange curve), RuO_2 (black curve). (c) and (d) Polarization curve of AEMWE tests of Pt/C || RuO_2 and Pt/C || $FeNi_3/FeNiO_x$ at 50 °C and 60 °C (without iR-correction).

allowing the simplest path from reactants to intermediates to products [49]. Consequently, the released hydrogen adsorption energy ΔG (H*) of electrocatalysts must be taken into account. The optimal value of ΔG (H*) adsorption should be close to the thermoneutral value, zero [50]. As reported by the computational study of Ni et all.'s [51] the ΔG (H*) for Ni_3Fe is 0.48 eV while the ΔG(H*) of platinum is very close to 0 eV, reflecting its excellent HER performance and making it a benchmark of cathode electrocatalysts over a wide pH range [51,29].

3.5. AEMWE test with electrocatalysts fully PGM-free

The complete single AEMWE cell performance using only $FeNi_3/FeNiO_x$ nanoparticles was obtained using an MEA having them as electrocatalyst at both anode and cathode side. This performance was compared with a MEA having Pt/C at the cathode electrocatalyst and RuO_2 at the anode electrocatalyst (Fig. 10). Also in this case, the polarization curves were acquired at two temperatures, 50 °C (Fig. 10a) and 60 °C (Fig. 10b) using 1 M KOH as support electrolyte. For both temperatures, the cell voltage with the PGM-free MEA remains comparable to that with the PGM up to approximately 150 mA cm^{-2}, and then remains lower throughout the scan. This is a sign that the slower kinetics for the HER reaction is compensated by the great ability of $FeNi_3/FeNiO_x$ in carrying out the OER reaction which, in the overall electrolysis process, is the kinetically decisive one involving four electrons [45]. The gap between the two curves increases by increasing the current density, in fact at 50 °C it goes from 114 mV at 0.4 A cm^{-2} up to 331 mV at 1 A cm^{-2} and at 60 °C it goes from 100 mV at 0.4 A cm^{-2} up to 284 mV at 1 A cm^{-2}, demonstrating the excellent operation of the PGM-free MEA at high current densities, with a voltage of 1.943 V at 1 A cm^{-2}.

The overall results obtained by the polarization curves at 50 °C and 60 °C with KOH 1 M as supporting electrolyte are summarized in Tables 1 and Table 2.

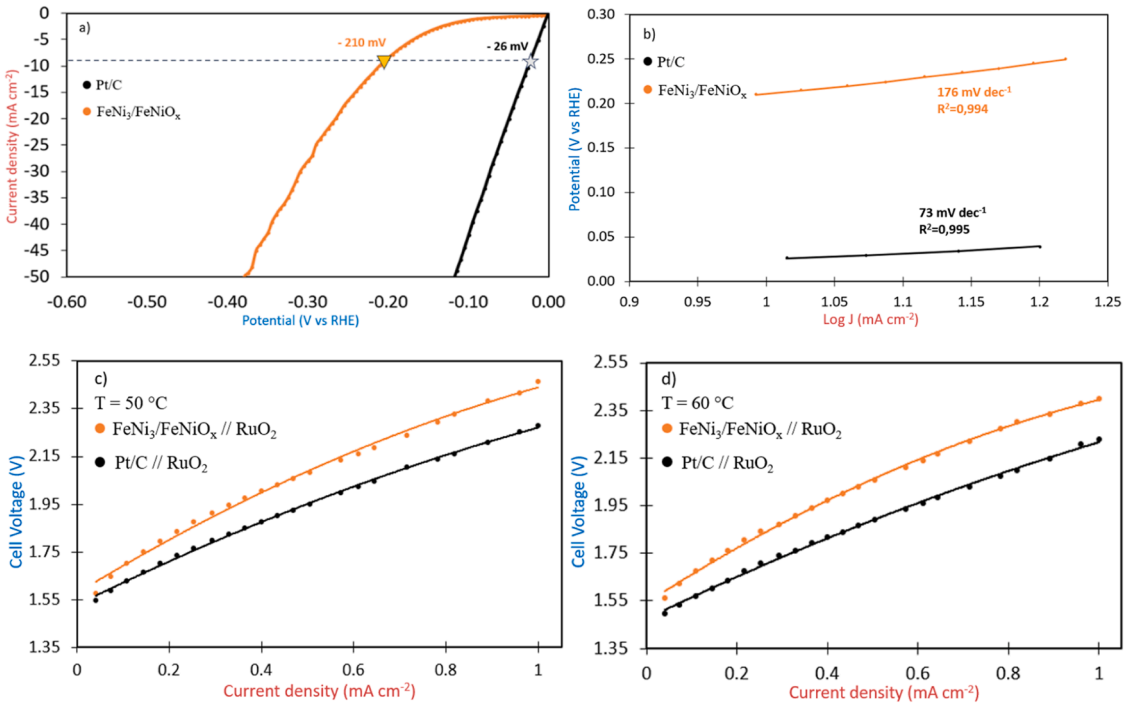

Fig. 8. **(a)** LSV comparison of HER electrocatalysts in 1.0 M KOH solution at a sweep rate of 5 mV s^{-1}: $FeNi_3/FeNiO_x$ (orange curve), Pt/C (black curve). **(b)** Tafel Plot comparison of HER electrocatalysts: $FeNi_3/FeNiO_x$ (orange curve), Pt/C (black curve). (c) and (d) Polarization curve of AEMWE tests of Pt/C || RuO_2 and $FeNi_3/FeNiO_x$ || RuO_2 at 50 °C and 60 °C (without iR-correction).

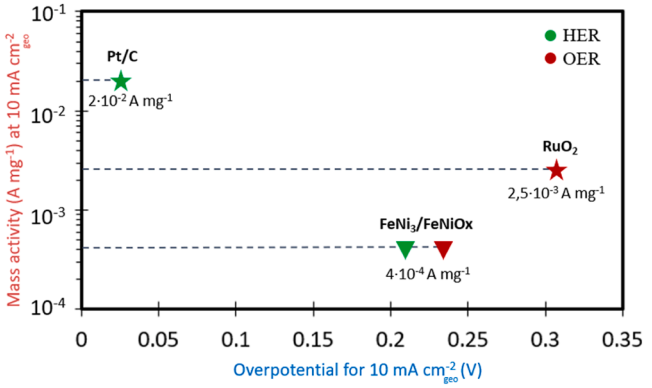

Fig. 9. Comparison of mass activity and overpotential at 10 mA cm^{-2} for HER and OER. Comparison of mass activity and overpotential at 10 mA cm^{-2} for HER and OER.

3.6. Degradation trend

An evaluation of the degradation trend of the MEA composed of $FeNi_3/FeNiO_x$ at both the anode and the cathode was carried out by investigating the effect of intermittent power supply. A daily power profile was chosen, instead of a continuous power supply for the entire

Table 1
Comparison of the electrocatalytic activities of noble and non-noble MEA employing in AEM cells at 50 °C **$FeNi_3/FeNiO_x$**.

Anode	Cathode	V at 0.4 A cm^{-2}	V at 0.6 A cm^{-2}	V at 1 A cm^{-2}
$FeNi_3/FeNiO_x$	**Pt/C**	1.626	1.713	1.867
RuO_2	**$FeNi_3/FeNiO_x$**	2.006	2.162	2.465
RuO_2	**Pt/C**	1.877	2.024	2.281
$FeNi_3/FeNiO_x$	**$FeNi_3/FeNiO_x$**	1.763	1.831	1.950

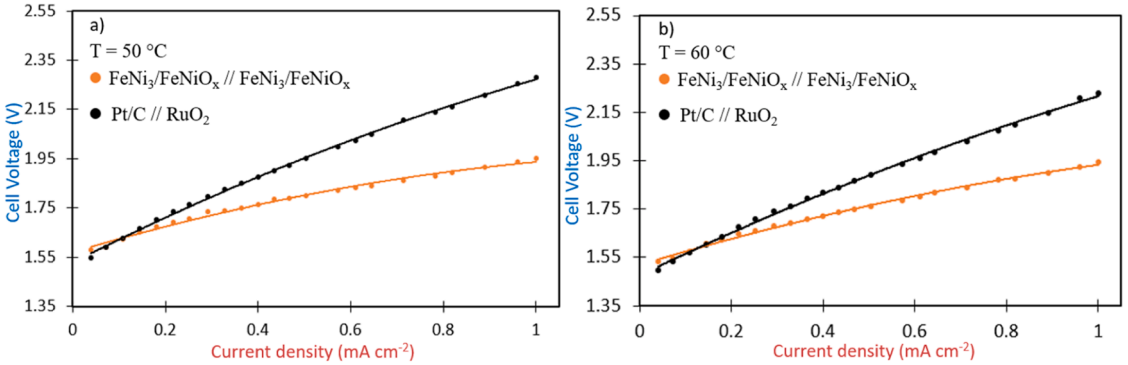

Fig. 10. **(a)** and **(b)** Polarization curve of AEMWE tests of Pt/C || RuO_2 and $FeNi_3/FeNiO_x$ || $FeNi_3/FeNiO_x$ at 50 °C and 60 °C (without iR-correction).

Table 2
Comparison of the electrocatalytic activities of noble and non-noble MEA employing in AEM cells at 60 °C.

Anode	Cathode	V at 0.4 A cm^{-2}	V at 0.6 A cm^{-2}	V at 1 A cm^{-2}
$FeNi_3$/ $FeNiO_x$	**Pt/C**	1.593	1.686	1.838
RuO_2	**$FeNi_3$/ $FeNiO_x$**	1.973	2.141	2.400
RuO_2	**Pt/C**	1.820	1.961	2.227
$FeNi_3$/ $FeNiO_x$	**$FeNi_3$/ $FeNiO_x$**	1.721	1.801	1.943

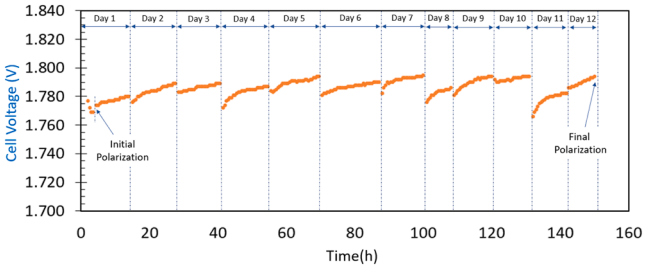

Fig. 11. Degradation trend of $FeNi_3/FeNiO_x$ MEA with an intermittent power supply.

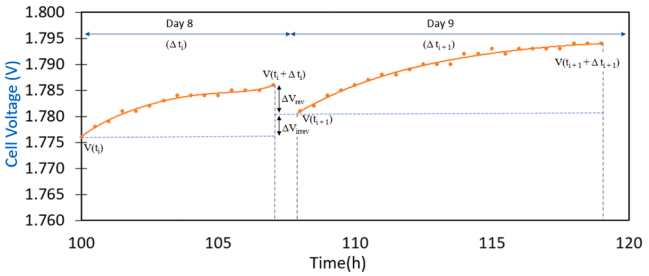

Fig. 12. Graphical definition of reversible and irreversible voltage losses of $FeNi_3/FeNiO_x$ MEA.

duration of the test, in order to best simulate the operation of the electrolyser when powered directly by renewable sources. The test was conducted with a current density of 0.4 A cm^{-2}, at 50 °C with 1 M KOH as supporting electrolyte. The daily power supply was varied between a minimum of 8 h and a maximum of 17.5 h, maintaining at least 8 h of OCV between one day and the next. Overall, the MEA was powered at a current density of 0.4 A cm^{-2} for 150 h, divided into 12 days (Fig. 11). Every day the MEA was activated at a current density of 0.2 A cm^{-2} for 1 h (not taken into consideration in the calculation of total operating hours and not reported in Fig. 11) in which a temporary lowering of the voltage was observed, probably due to decarbonization processes and changes in the oxidative states of the electrocatalysts. Although this test was conducted on a pilot-scale and provides information on degradation trends, it is not to be considered a definitive endurance test from an industrial point of view, where a wider range of conditions and hours should be evaluated.

The degradation rate was evaluated following the indications of the "EU harmonized protocols for testing low-temperature water electrolysers" [52] by calculating the reversible and irreversible voltage losses that can occur in tests involving consecutive shutdowns and restarts. According to the European document, reversible voltage losses U_{rev} means the sum, referring to each day of testing, of the difference between the voltage reached at the shout-down of one day and the starting voltage at the start-up of the following day. Following the graphic definitions given in Fig. 12, in which day 8 and 9 of our test were simplified

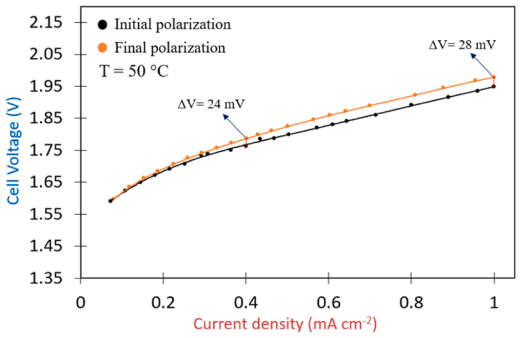

Fig. 13. Polarization curve of AEMWE tests of $FeNi_3/FeNiO_x$ || $FeNi_3/FeNiO_x$ before and after 150 h.

and taken as an example, the following formula can be reported Eq. (7):

$$U_{rev} = \frac{\sum_{i=1}^{N} V(t_i + \Delta t_i) - V(t_{i+1})}{\sum_{i=1}^{N} \Delta t_i} \quad (7)$$

The irreversible increase in the U_{irrev} voltage is instead defined as the sum, referring to each test day, of the difference between the starting voltage of one day and the starting voltage of the previous day. Once again, following the graphic definition in Fig. 12, the following formula can be reported Eq. (8):

$$U_{irrev} = \frac{\sum_{i=1}^{N} V(t_{i+1}) - V(t_i)}{\sum_{i=1}^{N} \Delta t_i} \quad (8)$$

The overall degradation rate U_{tot} Eq. (9) is the sum between the reversible and irreversible voltage loses:

$$U_{tot} = U_{rev} + U_{irrev} \quad (9)$$

In our case U_{rev} and U_{irrev} were 806 μV/h and 80 μV/h respectively, so the total degradation rate was 886 μV/h.

The loss of performance after 150 h was also evaluated by comparing the polarization curves obtained on the first and last day (Fig. 13). The voltage gap between the two curves was 24 mV and 28 mV at the current density of 0.4 A cm^{-2} and 1 A cm^{-2} respectively.

4. Perspective and outlook

Based on the analysis of the International Renewable Energy Agency (IRENA), to concretely make green hydrogen among the best low-carbon alternatives for energy reconversion, 5 terawatts (TW) of electrolysers installed capacity by 2050 will be needed. To achieve this large production of hydrogen it is necessary to focus efforts on the scale-up of electrolysers, with a significant reduction in costs, simplification and reduction of the environmental impact of their manufacturing [54]. For this reason, it is necessary to develop electrocatalysts obtainable from simple and scalable syntheses, which have good catalytic activity and durability despite not being composed of PGMs, which are not only scarce, but also among the most energy-intensive and emissive-intensive [55], consequently not suitable for large-scale production. It is in this perspective that this work moves: here it is presented not only the use of nickel and iron as metals, but a single and unchanged synthesis for both OER and HER electrocatalysts. Water is used as solvent and the reaction takes place at low temperature, with a single synthetic step followed an easy and fast work-up, fitting well with scale-up in batch reactors. In addition to the aforementioned synthetic advantages, the performances obtained for our PGM-free MEA are aligned with other PGM-free MEAs present in the literature, as shown in Table 3. Future studies will focus on research of chemical agents with the same reducing power and cost as hydrazine but which present fewer hazards for the environment and the health of operators. Another aspect that can be evaluated is the tuning of $FeNi_3/FeNiO_x$ to increase performance towards the HER, with a

Table 3
Comparison of the electrocatalytic activities of PGM-Free AEM cells.

Anode	Cathode	Membrane	Solution	V/I A cm^{-2}	T(°C)	
Ni_3Fe/NiFeO	Ni_3Fe/NiFeO	AT-100	1 M KOH	1.94/1	60	This work
NiMo	Fe-NiMo	Sustanion X37–50	1 M KOH	1.57/1	80	[26]
$CuCo_3$	Ni/CeO_2/La_2O_3	Tokuyama A201	K_2CO_3/$KHCO_3$	1.94/0.47	50	[43]
FePi-NiS	NiCoPi-NiS	FAA-3–50	1 M KOH	2.1/1	50	[53]
Fe_2P-$Ni_{12}P_5$	Co_2P-$Ni_{12}P_5$	FAA-3–50	1 M KOH	1.95/1	60	[28]
Ni/Mo_5N_6	Ni/Mo_5N_6	Sustanion X37–50	1 M KOH	1.57/1	80	[27]
$Co_{65}Fe_{35}O_XH_y$	$Co_{65}Fe_{35}O_XH_y$	Sustanion X37–50	1 M KOH	2/0.6	50	[44]

thoughtful evaluation of the costs and benefits between performance and scalability of the process, and an optimization of the quantity of electrocatalyst to be applied on the electrodes. A pilot scale cell was used for the electrolyzer tests but a more in-depth study on the electrocatalyst degradation should be conducted to evaluate the possible scale-up from a pilot plant to an industrial plant.

5. Conclusions

In summary, $FeNi_3$/$FeNiO_x$ nanoparticles were synthesized via simple and scalable chemical reduction with hydrazine. A characterization study was carried out using XRD, SEM, XPS, HR-TEM and HAADF-STEM and the electrocatalytic activity of $FeNi_3$/$FeNiO_x$ for both HER and OER was evaluated by LSV, Tafel slop, and AEMWE single-cell tests. The performances were compared with commercial PGM-based Benchmarks electrocatalysts, considering the mass activity and the geometrical activity. The electrocatalyst exhibits an overpotential of 210 mV and 234 mV for HER and OER respectively, at a current density of 10 mA cm^{-2} in 1 M KOH. Our PGM-free MEA, consisting of a single electrocatalyst, outperform the totally PGM-based one and is aligned with other PGM-free MEAs present in the literature. In a pilot-scale single cell tests, the MEA reaches a voltage (without iR-correction) of 1.72 V and 1.94 V at a current density of 0.4 A cm^{-2} and 1 A cm^{-2} respectively at 60 °C; with a voltage gap of 284 mV at 1 A cm^{-2} in comparison to the PGMs one, and it was tested for 150 h with a daily power profile simulating that of renewable sources; the degradation rate was 886 μV/h. This study developed an effective strategy to design an efficient non-precious metal-based MEA, composed of a single electrocatalyst, for green hydrogen production.

CRediT authorship contribution statement

Francesko Malaj: Writing – review & editing, Writing – original draft, Methodology, Investigation, Formal analysis, Data curation, Conceptualization. **Alessandro Tampucci:** Writing – review & editing, Writing – original draft, Methodology, Investigation, Conceptualization. **Domenico Lentini:** Writing – original draft, Methodology, Investigation, Formal analysis, Data curation, Conceptualization. **Lorenzo Brogi:** Writing – original draft, Methodology, Investigation. **Enrico Berretti:** Writing – review & editing, Writing – original draft, Methodology, Investigation, Formal analysis, Data curation. **Camilla Coletti:** Writing – original draft, Methodology, Investigation, Formal analysis, Data curation. **Stiven Forti:** Writing – original draft, Methodology, Investigation, Formal analysis, Data curation. **Antonio Rossi:** Writing – original draft, Methodology, Investigation, Formal analysis, Data curation. **Carlo Santoro:** Writing – review & editing, Writing – original draft, Methodology, Investigation, Formal analysis, Data curation, Conceptualization.

Declaration of competing interest

The authors declare that they have no known competing financial interests or personal relationships that could have appeared to influence the work reported in this paper.

Data availability

Data will be made available on request.

Supplementary materials

Supplementary material associated with this article can be found, in the online version, at doi:10.1016/j.electacta.2024.145109.

References

[1] A.M. Oliveira, R.R. Beswick, Y. Yan, A green hydrogen economy for a renewable energy society, Curr. Opin. Chem. Eng. 33 (2021), https://doi.org/10.1016/j.coche.2021.100701. Preprint at.
[2] J. Chi, H. Yu, Water electrolysis based on renewable energy for hydrogen production, Cuihua Xuebao/Chinese J. Catalysis 39 (2018) 390–394, https://doi.org/10.1016/S1872-2067(17)62949-8. Preprint at.
[3] M. El-Shafie, Hydrogen production by water electrolysis technologies: a review, Results Eng. 20 (2023).
[4] S. Shiva Kumar, V. Himabindu, Hydrogen production by PEM water electrolysis – A review, Mater. Sci. Energy Technol. 2 (2019) 442–454, https://doi.org/10.1016/j.mset.2019.03.002. Preprint at.
[5] J. Brauns, T. Turek, Alkaline water electrolysis powered by renewable energy: a review, Processes 8 (2020), https://doi.org/10.3390/pr8020248. Preprint at.
[6] I. Vincent, D. Bessarabov, Low cost hydrogen production by anion exchange membrane electrolysis: a review, Renew. Sustain. Energy Rev. 81 (2018) 1690–1704, https://doi.org/10.1016/j.rser.2017.05.258. Preprint at.
[7] M.I. Jamesh, X. Sun, Recent progress on earth abundant electrocatalysts for oxygen evolution reaction (OER) in alkaline medium to achieve efficient water splitting – A review, J. Power Sources 400 (2018) 31–68, https://doi.org/10.1016/j.jpowsour.2018.07.125. Preprint at.
[8] L. Trotochaud, S.L. Young, J.K. Ranney, S.W. Boettcher, Nickel-Iron oxyhydroxide oxygen-evolution electrocatalysts: the role of intentional and incidental iron incorporation, J. Am. Chem. Soc. 136 (2014) 6744–6753.
[9] M. Gong, H. Dai, A mini review of NiFe-based materials as highly active oxygen evolution reaction electrocatalysts, Nano Res. 8 (2015) 23–39, https://doi.org/10.1007/s12274-014-0591-z. Preprint at.
[10] X. Yan, et al., FeNi3/NiFeOx nanohybrids as highly efficient bifunctional electrocatalysts for overall water splitting, Adv Mater Interfaces 3 (2016).
[11] J. Mohammed-Ibrahim, S. Xiaoming, Recent progress on earth abundant electrocatalysts for hydrogen evolution reaction (HER) in alkaline medium to achieve efficient water splitting – A review, J. Energy Chem. 34 (2019) 111–160, https://doi.org/10.1016/j.jechem.2018.09.016. Preprint at.
[12] Y. Lee, J. Suntivich, K.J. May, E.E. Perry, Y. Shao-Horn, Synthesis and activities of rutile IrO 2 and RuO 2 nanoparticles for oxygen evolution in acid and alkaline solutions, J. Phys. Chem. Lett. 3 (2012) 399–404, https://doi.org/10.1021/jz2016507. Preprint at.
[13] M.B. Kale, R.A. Borse, A. Gomaa Abdelkader Mohamed, Y. Wang, Electrocatalysts by Electrodeposition: recent Advances, Synthesis Methods, and Applications in Energy Conversion, Adv. Funct. Mater. 31 (2021), https://doi.org/10.1002/adfm.202101313. Preprint at.
[14] J. Lian, Y. Wu, J. Sun, High current density electrodeposition of NiFe/Nickel Foam as a bifunctional electrocatalyst for overall water splitting in alkaline electrolyte, J. Mater. Sci. 55 (2020) 15140–15151.

[15] E. Hatami, A. Toghraei, G. Barati Darband, Electrodeposition of Ni–Fe micro/nano urchin-like structure as an efficient electrocatalyst for overall water splitting, Int. J. Hydrogen Energy 46 (2021) 9394–9405.

[16] Q. Luo, M. Peng, X. Sun, Y. Luo, A.M. Asiri, Efficient electrochemical water splitting catalyzed by electrodeposited NiFe nanosheets film, Int. J. Hydrogen Energy 41 (2016) 8785–8792.

[17] Y. Wang, et al., Industrially promising IrNi-FeNi3 hybrid nanosheets for overall water splitting catalysis at large current density, Appl. Catal. B 286 (2021).

[18] M. Guo, H. Meng, J. Jin, J. Mi, Amine-assisted synthesis of the Ni3Fe alloy encapsulated in nitrogen-doped carbon for high-performance water splitting, J Mater Chem A Mater 11 (2023) 6452–6464.

[19] R. Xin, et al., Low-temperature pyrolysis enables FeNi3 nanoparticle implanted N-doped carbon nanosheets as an efficient bifunctional electrocatalyst for overall water splitting, J. Mater. Chem. A Mater. 11 (2023) 14015–14024.

[20] Q. Zhou, et al., Duplex interpenetrating-Phase FeNiZn and FeNi3 heterostructure with low-gibbs free energy interface coupling for highly efficient overall water splitting, Nanomicro. Lett. 15 (2023).

[21] G. Wei, et al., Hexagonal Phase Ni3Fe nanosheets toward high-performance water splitting by a room-temperature methane plasma method, Adv. Funct. Mater. 32 (2022).

[22] G.N. Glavee, K.J. Klabunde, lb M. Christopher Sorensen, G.C. Hadjipanayis, Chemistry of Borohydride Reduction of Iron(II) and Iron(III) Ions in Aqueous and Nonaqueous Media. Formation of Nanoscale Fe, FeB, and FeaB Powders, Inorg. Chem 34 (1995). https://pubs.acs.org/sharingguidelines.

[23] Z. Liu, et al., Efficient overall water splitting catalyzed by robust FeNi3N nanoparticles with hollow interiors, J. Mater. Chem. A Mater. 9 (2021) 7750–7758.

[24] Z. Li, et al., Synergistic coupling of FeNi3 alloy with graphene carbon dots for advanced oxygen evolution reaction electrocatalysis, J. Colloid Interface Sci. 615 (2022) 273–281.

[25] X. Lu, G. Liang, Y. Zhang, Synthesis and characterization of magnetic FeNi3 particles obtained by hydrazine reduction in aqueous solution, Mater. Sci. Eng.: B 139 (2007) 124–127.

[26] P. Chen, X. Hu, High-efficiency anion exchange membrane water electrolysis employing non-noble metal catalysts, Adv. Energy Mater. 10 (2020).

[27] H. Wang, Y. Tong, K. Li, P. Chen, Heterostructure engineering of iridium species on nickel/molybdenum nitride for highly-efficient anion exchange membrane water electrolyzer, J. Colloid Interface Sci. 628 (2022) 306–314.

[28] L. Guo, et al., Self-supported bimetallic phosphide heterojunction-integrated electrode promoting high-performance alkaline anion-exchange membrane water electrolysis, ACS Sustain. Chem. Eng. 10 (2022) 9956–9968.

[29] A.H. Faqeeh, M.D. Symes, A standard electrolyzer test cell design for evaluating catalysts and cell components for anion exchange membrane water electrolysis, Electrochim. Acta 444 (2023).

[30] Y. Sugawara, et al., Anion exchange membrane water electrolyzers: an overview, J. Chem. Eng. Jpn. 56 (2023).

[31] Z. Li, C. Han, J. Shen, Reduction of Ni2+ by hydrazine in solution for the preparation of nickel nano-particles, J. Mater. Sci. 41 (2006) 3473–3480.

[32] R. Eluri, B. Paul, Development and dispensing of a nickel nanoparticle ink for the diffusion brazing of a microchannel array, J. Nanopart. Res. 15 (2013).

[33] S. Anantharaj, S. Noda, Amorphous catalysts and electrochemical water splitting: an untold story of harmony, Small 16 (2020), https://doi.org/10.1002/smll.201905779. Preprint at.

[34] W. Cai, et al., Amorphous versus crystalline in water oxidation catalysis: a case study of NiFe Alloy, Nano Lett. 20 (2020) 4278–4285.

[35] S. Thoufeeq, et al., Single step grown NiFe sponges as efficient water splitting electrocatalysts in alkaline medium, Chem. Select. 5 (2020) 1385–1395.

[36] J. Liu, et al., Supra hydrolytic catalysis of Ni3Fe/rGO for hydrogen generation, Adv. Sci. 9 (2022).

[37] M.C. Biesinger, et al., Resolving surface chemical states in XPS analysis of first row transition metals, oxides and hydroxides: cr, Mn, Fe, Co and Ni, Appl. Surf. Sci. 257 (2011) 2717–2730.

[38] A.P. Grosvenor, B.A. Kobe, M.C. Biesinger, N.S. McIntyre, Investigation of multiplet splitting of Fe 2p XPS spectra and bonding in iron compounds, Surf. Interface Anal. 36 (2004) 1564–1574.

[39] A.P. Grosvenor, M.C. Biesinger, R.S.C. Smart, N.S. McIntyre, New interpretations of XPS spectra of nickel metal and oxides, Surf. Sci. 600 (2006) 1771–1779.

[40] M.C. Biesinger, B.P. Payne, L.W.M. Lau, A. Gerson, R.S.C. Smart, X-ray photoelectron spectroscopic chemical state Quantification of mixed nickel metal, oxide and hydroxide systems, Surf. Interface Anal. 41 (2009) 324–332.

[41] Z.P. Wu, X.F. Lu, S.Q. Zang, X.W. Lou, Non-noble-metal-based electrocatalysts toward the oxygen evolution reaction, Adv. Funct. Mater. 30 (2020), https://doi.org/10.1002/adfm.201910274. Preprint at.

[42] J. Zhao, J.J. Zhang, Z.Y. Li, X.H. Bu, Recent progress on NiFe-based electrocatalysts for the oxygen evolution reaction, Small 16 (2020), https://doi.org/10.1002/smll.202003916. Preprint at.

[43] C.C. Pavel, et al., Highly efficient platinum group metal free based membrane-electrode assembly for anion exchange membrane water electrolysis, Angewandte Chemie - International Edition 53 (2014) 1378–1381.

[44] S. Hong, H. Kim, H.W. Jang, S.Y. Kim, S.H. Ahn, An electrochemically fabricated cobalt iron oxyhydroxide bifunctional electrode for an anion exchange membrane water electrolyzer, Dalton Trans. 52 (2023) 6324–6330.

[45] N.T. Suen, et al., Electrocatalysis for the oxygen evolution reaction: recent development and future perspectives, Chem. Soc. Rev. 46 (2017) 337–365, https://doi.org/10.1039/c6cs00328a. Preprint at.

[46] Y. Yang, H. Fei, G. Ruan, C. Xiang, J.M. Tour, Efficient electrocatalytic oxygen evolution on amorphous nickel-cobalt binary oxide nanoporous layers, ACS Nano 8 (2014) 9518–9523.

[47] M.D. Struble, M.T. Scerba, M. Siegler, T. Lectka, Evidence for a symmetrical fluoronium ion in solution, Science (1979) 340 (2013) 57–60.

[48] W.D. Chemelewski, H.C. Lee, J.F. Lin, A.J. Bard, C.B. Mullins, Amorphous FeOOH oxygen evolution reaction catalyst for photoelectrochemical water splitting, J. Am. Chem. Soc. 136 (2014) 2843–2850.

[49] M. Ďurovič, J. Hnát, K. Bouzek, Electrocatalysts for the hydrogen evolution reaction in alkaline and neutral media. A comparative review, J. Power Sources 493 (2021), https://doi.org/10.1016/j.jpowsour.2021.229708. Preprint at.

[50] Y. Hu, et al., Enhanced metallicity boosts hydrogen evolution capability of dual-bimetallic Ni–Fe nitride nanoparticles, Mater. Today Phys. 15 (2020).

[51] Y. Ni, et al., Ultralow-content Pt nanodots/Ni3Fe nanoparticles: interlayer nanoconfinement synthesis and overall water splitting, Nanoscale (2024), https://doi.org/10.1039/d4nr00029c.

[52] Tsotridis, G. & Pilenga, A. EU harmonised protocols for testing of low temperature water electrolysers. in (2021). doi:10.2760/58880.

[53] L. Guo, et al., Self-supported crystalline-amorphous composites of metal phosphate and NiS for high-performance water electrolysis under industrial conditions, Appl. Catal. B 340 (2024).

[54] IRENA. Green Hydrogen Cost Reduction: Scaling up Electrolysers to Meet the 1.5^{0}C Climate Goal, International Renewable Energy Agency, Abu Dhabi, 2020.

[55] P. Nuss, M.J. Eckelman, Life cycle assessment of metals: a scientific synthesis, PLoS One 9 (2014).

[56] C. Liang, et al., Highly conductive and mechanically robust NiFe alloy aerogels: an exceptionally active and durable water oxidation catalyst, Small 18 (2022).

[57] J.V. Acrivos, N.F. Mott, A.D. Yoffe, Physics and Chemistry of Electrons and Ions in Condensed Matter. Nato Science Series C: ASIC 130, 1984.

[58] J. Kibsgaard, I. Chorkendorff, Considerations for the scaling-up of water splitting catalysts, Nature Energy 4 (2019) 430–433, https://doi.org/10.1038/s41560-019-0407-1. Preprint at.